The influence of the iron content on the reductive decomposition of A 3−x Fe x Al 2 Si 3 O 12 garnets (A = Mg, Mn; 0.47 ≤ x ≤ 2.85)

Claudia Aparicio, Jan Filip, Miroslav Mashlan, and Radek Zboril

Citation: AIP Conference Proceedings **1622**, 12 (2014); doi: 10.1063/1.4898606
View online: http://dx.doi.org/10.1063/1.4898606
View Table of Contents: http://scitation.aip.org/content/aip/proceeding/aipcp/1622?ver=pdfcov
Published by the AIP Publishing

The Influence of the Iron Content on the Reductive Decomposition of $A_{3-x}Fe_xAl_2Si_3O_{12}$ Garnets (A = Mg, Mn; $0.47 \leq x \leq 2.85$)

Claudia Aparicio,[a] Jan Filip, Miroslav Mashlan, and Radek Zboril

Regional Centre of Advanced Technologies and Materials, Departments of Experimental Physics and Physical Chemistry, Faculty of Science, Palacky University, 17. listopadu 1192/12, 77146 Olomouc, Czech Republic

[a] Corresponding author: claudia.aparicio@upol.cz

Abstract. Thermally-induced reductive decomposition of natural iron-bearing garnets of the almandine-pyrope and almandine-spessartine series were studied at temperatures up to 1200 °C (heating rate of 10 °C/min) under atmosphere of forming gas (10% of H_2 in N_2). Crystallochemical formula of the studied garnet was calculated as $^{VIII}(A_{3-x}Fe^{2+}_x)^{VI}(Al, Fe^{3+})_2Si_3O_{12}$, where the amount of Fe^{3+} in the octahedral sites is negligible with the exception of pyrope, A = Mg, Mn, and $0.47 \leq x \leq 2.85$. The observed decomposition temperature, determined from differential scanning calorimetry and thermogravimetry, is greater than 1000 °C in all cases and showed almost linear dependence on the iron content in the dodecahedral sites of the studied garnets, with the exception of garnet with a near-pyrope composition ($Prp_{80}Alm_{20}$). The initial garnet samples and decomposition products were characterized in details by means of X-ray powder diffraction and ^{57}Fe Mössbauer spectroscopy. We found that all studied garnets have common decomposition products such as metallic iron (in general, rounded particles below 4 μm) and Fe-spinel; the other identified decomposition products depend on starting chemical composition of the garnet: Fe-cordierite, olivine (fayalite or tephroite), cristobalite, pyroxene (enstatite or pigeonite), and anorthite. Anorthite and pigeonite were only present in garnets with Ca in the dodecahedral site. All the identified phases were usually well crystallized.

Keywords: Fe-bearing garnets, thermal behavior, reducing atmosphere, iron particles, Mössbauer spectroscopy.
PACS: 76.80.+y, 81.40.-z, 81.70.Pg, 82.30.Lp, 82.80.Ej.

INTRODUCTION

Garnet is an important group of aluminosilicate minerals; these minerals are widespread in the Earth's crust and upper mantle as the major rock-forming mineral. In petrology, they are frequently used as geobarometers to understand the P-T history of rock assemblage, which involve many equilibrium reactions occurring in the Earth's upper mantle [1,2]. Because of these multiple reactions, natural garnets are rarely found as pure end-members. In industrial applications, garnets are promising materials owing to their hardness and specific gravity. The most important uses of garnet include abrasives in coarse and fine polishing, sand blasting, water jet cutting, and water filtration [1,3]; other uses are as anti-skid material, spark-plug cleaning, and gems [4].

Garnet with a cubic structure and space group Ia-3d has a structural formula $^{VIII}X_3{}^{VI}Y_2{}^{IV}Z_3O_{12}$, where $X = Fe^{2+}$, Mg^{2+}, Mn^{2+}, Ca^{2+}, $Y = Fe^{3+}$, Ti^{3+}, Cr^{3+}, Al^{3+}, and $Z = Si^{4+}$; the roman number superscripts indicate the coordination number for each particular site [5,6]. There are several garnets compositions, and, commonly, they form chemically restricted series (*i.e.*, solid solutions), *e.g.*, almandine-pyrope ($Fe_3Al_2Si_3O_{12}$ - $Mg_3Al_2Si_3O_{12}$) or almandine-spessartine ($Mg_3Al_2Si_3O_{12}$ - $Mn_3Al_2Si_3O_{12}$).

The garnet properties has been widely studied, especially those from garnets belonging to the almandine-pyrope series, including their electrical [7], magnetic [8,9], and thermodynamic properties [10]. Only few of these studies have focused on garnet thermal decomposition, the majority of them in air or vacuum. Based on these studies, garnets decompose at high temperatures between 750 and 1200 °C, and the decomposition products vary according

Mossbauer Spectroscopy in Materials Science - 2014
AIP Conf. Proc. 1622, 12-23 (2014); doi: 10.1063/1.4898606

to the initial composition of garnet and the atmosphere of reaction; also, they are susceptible to changes in pressure [11,12]. For example, the decomposition products of almandine in oxidative atmosphere involve iron oxides (hematite or magnetite), hercynite, sillimanite, and silicon oxide (quartz or cristobalite) [11,13]. Detailed studies on thermal decomposition of garnet using Mössbauer spectroscopy [14,15] demonstrated that maghemite (γ-Fe_2O_3) is the original product of almandine decomposition on air at temperatures higher than 750 °C and it is subsequently transformed to ε-Fe_2O_3 and finally to hematite (α-Fe_2O_3). In a close system, almandine decomposes into hercynite, Fe-cordierite, and fayalite when heated between 750 °C and 1050 °C during several days [16].

Garnets of pyrope-almandine solid solution heated up to 1200 °C in air decompose into spinel ($Mg(Al,Fe^{3+})_2O_4$), anorthite, and enstatite when they have composition close to pyrope, while cordierite, anorthite, and spinel or maghemite were detected after the decomposition of garnet of almandine-pyrope intermediate composition [17]. Thermal decomposition of ideal end-member pyrope, in air, gives corundum and enstatite as decomposition products [13], and when pyrope contains Fe^{2+} in the dodecahedral sites, the decomposition products are enstatite, Fe-spinel, cristobalite, and hematite; hematite is a product of subsequent oxidation of enstatite at high temperature [18]. Thermal decomposition of intermediate garnet composition was also studied in nitrogen atmosphere, and above 900 °C, cordierite, spinel, and olivine or pyroxene were observed; the presence of clinopyroxene was reported in the case of decomposition of Ca-rich garnets [16].

From the literature review, we can infer that iron presence in garnet dodecahedral sites seems to be an important factor on the thermal decomposition mechanism. Therefore, in this paper we have focused on the study of the relationship between the iron content in natural garnets and its thermal behavior under reducing atmosphere up to 1200 °C, as a continuation of our previous studies [19,20].

EXPERIMENTAL DETAILS

Description of Natural-Garnet Samples

The color of the garnets used in this study vary from brownish-red and red for garnet compositions near to end-member almandine and pyrope, respectively; all crystals are almost free of impurities and they are transparent and slightly colored under optical microscope.

Electron microprobe analysis (EMPA) was performed on starting garnet samples in order to determine their chemical composition. For these analysis, a Cameca SX100 electron microprobe was employed, operating in the wavelength dispersive mode with an accelerating voltage of 15 kV, a beam current of 20 nA, and analytical spot size of ~1 μm. The following standards and analytical spectral lines were used: K_α lines: sanidine (Si, Al, K), albite (Na), almandine (Fe), pyrope (Mg), andradite (Ca), rhodonite (Mn), rutile (Ti), $ScVO_4$ (Sv, V); L_α lines: pollucite (Cs), Rb-leucite (Rb). The analytical data were corrected using the PAP correction procedure [21] and normalized to 12 anions per formula unit. The averaged results of EMPA analysis yielded a crystallochemical formula as given in Table 1, ignoring the minor components in the structure.

TABLE 1. Crystallochemical formulas of garnets with cations normalized to twelve oxygens.

Sample	Crystallochemical formula
$Prp_{80}Alm_{20}$	$(Mg_{2.22}Fe_{0.47}Ca_{0.33})(Cr_{0.11}Fe_{0.07}Al_{1.81})Si_{2.98}O_{12}$
$Prp_{36}Alm_{64}$	$(Mg_{1.04}Fe_{1.87}Ca_{0.09})(Al_{1.99})Si_{2.98}O_{12}$
$Prp_{18}Alm_{82}$	$(Mg_{0.51}Fe_{2.34}Mn_{0.11}Ca_{0.06})(Al_{2.00})Si_{2.97}O_{12}$
Prp_4Alm_{96}	$(Mg_{0.15}Fe_{2.85})(Al_{1.99})Si_{2.99}O_{12}$
$Sps_{35}Alm_{65}$	$(Mn_{1.09}Fe_{1.95})(Al_{1.99})Si_{2.94}O_{12}$

Sample Preparation and Characterization Techniques

Under the optical microscopy, small pieces of garnet crystal free of impurities were selected. The pieces were then ground in an agate mortar under isopropyl alcohol and air dried at room temperature. The samples were labelled as $Prp_{80}Alm_{20}$, $Prp_{36}Alm_{64}$, $Prp_{18}Alm_{82}$, Prp_4Alm_{96}, and $Sp_{35}Alm_{65}$ (see Table 1).

Both thermogravimetric analysis (TG) and differential scanning calorimetry (DSC) were carried out in a simultaneous thermal analyzer (STA 449 C Jupiter, Netzsch), coupled to mass spectrometer (QMS 403 Aëolos,

Netzch) for evolved gas analysis (EGA). The samples were individually heated from room temperature to 1200 °C, under the reducing atmosphere of forming gas (H_2 10%, N_2 90%) with a heating rate of 10 K/min in an open alumina crucible. Once the selected temperature was reached, the samples were cooled down to room temperature under inert atmosphere of argon, with a heating rate of – 40 K/min. The samples resulting from the heating process were labelled as follow: $Prp_{80}Alm_{20}$-1200, $Prp_{36}Alm_{64}$-1200, $Prp_{18}Alm_{82}$-1200, Prp_4Alm_{96}-1200, and $Sp_{35}Alm_{65}$-1200.

X-ray powder diffraction (XRD) and ^{57}Fe Mössbauer spectroscopy were employed to identify the present phases in all the samples (*i.e.*, before and after dynamic thermal treatment). XRD patterns were recorded at room temperature using an X'Pert PRO MPD diffractometer (PANalytical) with Co-K_α radiation and step size of 0.017° in the Bragg-Brentano geometry. Complementary XRD measurements at high temperature (*in situ*) were performed on $Prp_{80}Alm_{20}$ sample to monitor the decomposition products at very beginning of the decomposition reaction. Same model of diffractometer was used equipped with an Anton Paar HTK-16 reaction chamber; the Bragg-Brentano geometry was used with a step size of 0.017° and angular range (2θ) from 15 to 85°, the collection time of each diffractogram was set to 45 min with a sampling time of 0.30 s/step. The garnet sample was placed directly on a platinum holder. The heating and cooling rates were 10 K/min and – 100 K/min, respectively; the temperature range was from 500 to 1200 °C, the diffractograms were collected every 50 °C until a temperature of 1050 °C was reached; afterwards, the collection took place every 10 °C. The measurements were performed under reducing atmosphere of forming gas. The identification of crystalline phases and Rietveld refinement on collected XRD patterns were performed using the X'Pert High Score Plus software together with PDF-4+ and ICSD databases.

^{57}Fe Mössbauer spectra were collected at room temperature (RT) in a constant acceleration regime with a ^{57}Co(Rh) source with 1024 channels. The isomer shift values were calibrated with respect to α-Fe foil; CONFIT2000 software was used to fit the spectra.

Scanning electron microscopy (SEM) was performed on each sample prepared by thermal treatment to study the morphology of decomposition products. The SEM images were obtained using a Hitachi SU-6600 microscope.

RESULTS AND DISCUSSION

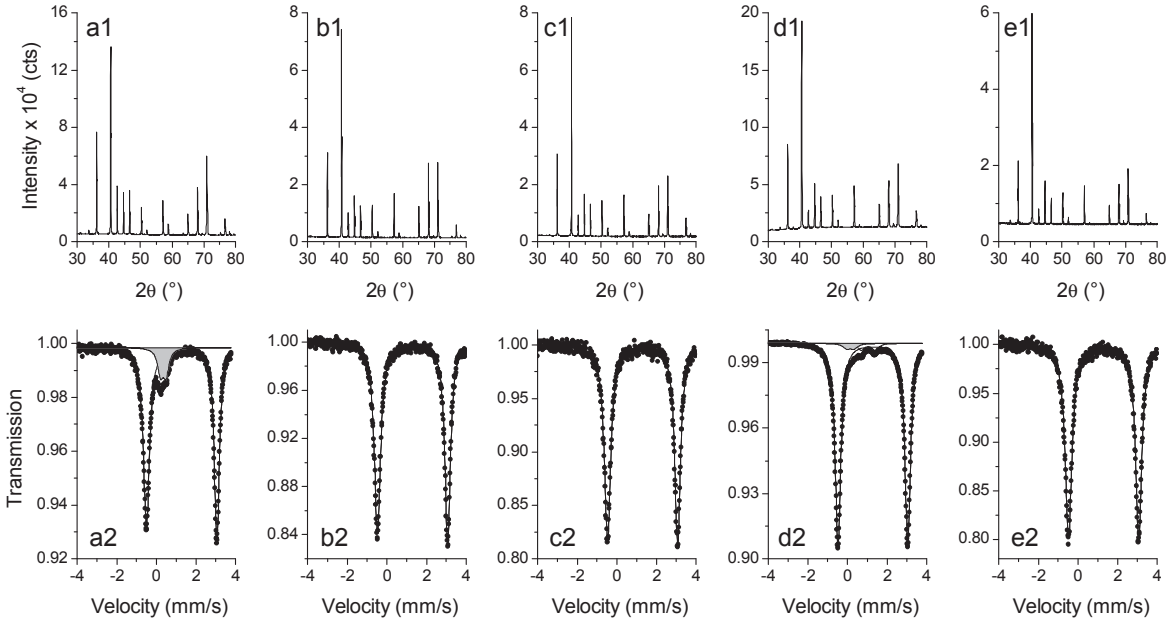

FIGURE 1. XRD patterns (top) and room temperature ^{57}Fe Mössbauer spectra (bottom) of natural garnets without any previous thermal treatment: (a) $Prp_{80}Alm_{20}$, (b) $Prp_{36}Alm_{64}$, (c) $Prp_{18}Alm_{82}$, (d) Prp_4Alm_{96}, and (e) $Sps_{35}Alm_{65}$.

Garnet samples were characterized by XRD and Mössbauer spectroscopy. All diffractograms (see Fig. 1) show typical patterns for garnet structure. ^{57}Fe Mössbauer spectra taken at room temperature (see Fig. 1) were fitted with

one doublet with Mössbauer parameters characteristic of Fe^{2+} in a garnet, *i.e.*, isomer shift (IS): 1.28–1.30 mm/s and quadrupole splitting (QS): 3.52–3.55 mm/s [22,23]. Exceptions are spectra of $Prp_{80}Alm_{20}$ and Prp_4Alm_{96} samples, which were fitted with two doublets and three doublets, respectively. All the samples are free of impurities; only Prp_4Alm_{96} contains a small amount of ilmenite ($FeTiO_3$, ~4%, according to the doublet area) in accordance with the XRD pattern. The doublets for Fe^{2+} display certain degree of asymmetry; this is more pronounced in Mössbauer spectrum of $Prp_{80}Alm_{80}$ sample, which has a lower concentration of iron.

Variation of Onset Temperature with Respect to the Fe Content in Garnets

According to TGA and EGA (not shown here), all the studied samples showed a small release of water before thermal decomposition; in most of the cases, there were fluid inclusions in the crystalline garnet or moisture of the sample. Only in the case of almandine (Prp_4Alm_{96}), a fraction of the released water corresponded to the thermal decomposition of mineral impurities (ilmenite) [20]. TG curves show evident decreases in mass after the beginning of thermal decomposition; they seem to be a "one-step" process, with exception for $Prp_{80}Alm_{20}$ that shows two-steps. The mass loss (Δm_{exp}) at the end of TG analysis is different for each garnet (see Table 2).

TABLE 2. Onset temperatures and mass decrease (experimental and theoretical values) of garnets with different contents of iron in X-site.

Sample	X[Fe]	Onset (°C)	Δm_{exp} (wt. %)	Δm_{th} (wt. %)
$Prp_{80}Alm_{20}$	0.465(05)	1087	– 0.69	n.c.
$Prp_{36}Alm_{64}$	1.864(16)	1131	– 4.33	– 4.26
$Prp_{18}Alm_{82}$	2.339(11)	1103	– 2.00	– 1.97
Prp_4Alm_{96}	2.854(11)	1045	– 3.51	– 3.57*
$Sps_{35}Alm_{65}$	1.946(88)	1125	– 1.34	– 1.34

n.c. = not calculated, * 2 wt% of ilmenite inclusions was considered.

DSC analysis (Fig. 2a) shows sharp endothermic peaks indicating the decomposition process of the garnet. With exception of pyrope ($Prp_{80}Alm_{20}$), all garnets showed one endothermic peak at temperatures greater than 1000 °C but less than 1200 °C, which is similar to the decomposition temperatures found in experiments under oxidative atmosphere [13,17,18]. From these peaks, it was possible to calculate the onset temperature of thermal decomposition for each garnet (see Table 2).

Onset temperature of decomposition from Prp-Alm series shows a negative linear correlation with the increase of iron content in the dodecahedral sites of the garnet (Fig. 2b); $Sps_{35}Alm_{65}$ garnet falls on the same line. However, the sample with the least content of iron ($Prp_{80}Alm_{20}$) does not follow this trend; instead, it has a lower onset temperature than garnets of intermediate composition, but around 40 °C greater than that for almost pure almandine (Prp_4Alm_{96}). The $Prp_{80}Alm_{20}$ sample also shows a slower decomposition rate than that observed for other samples.

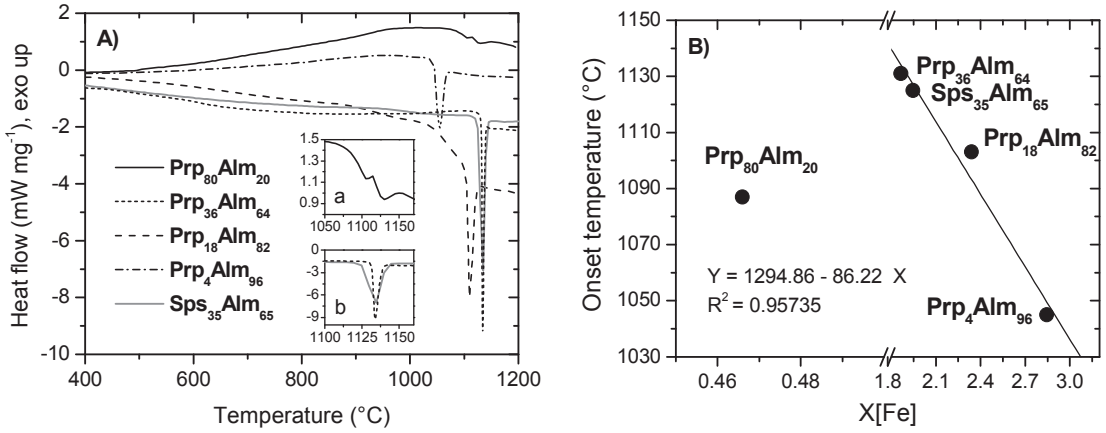

FIGURE 2. (A) DSC heating curves of the studied natural garnets, showing the endothermic peaks of decomposition. Insets: (a) detail view of the endothermic effects of Prp_4Alm_{96}, (b) detail view of the curve for $Prp_{36}Alm_{64}$ and $Sps_{35}Alm_{65}$ garnets. (B) Variation of the onset temperature, calculated from DSC, with respect to the iron content in garnet (dodecahedral positions).

The lowest temperature of decomposition was observed in the case of the garnet with a composition close to almandine, which could be explained in terms of the induced iron reduction. In contrast, the garnet with a composition close to pyrope, presents not only Fe^{3+} and Cr^{3+} in the octahedral sites, but also Ca^{2+} in the dodecahedral sites, which might increase the instability of the lattice at high temperatures [24,25]. The ferric ions reduce to ferrous ions, but, apparently, they do not stay in the same octahedral site as there was no evidence in the Mössbauer spectra, where it is not possible to ascribe any doublet to Fe^{2+} in the octahedral site. The other factor controlling the instability of $Prp_{80}Alm_{20}$ garnet involves the different ion size of Ca^{2+} (1.12 Å), Fe^{2+} (0.92 Å), and Mg^{2+} (0.89 Å), which could increase the strain and distortion of the garnet lattice, affecting not only the dodecahedral sites, but also the octahedral and even tetrahedral sites [26].

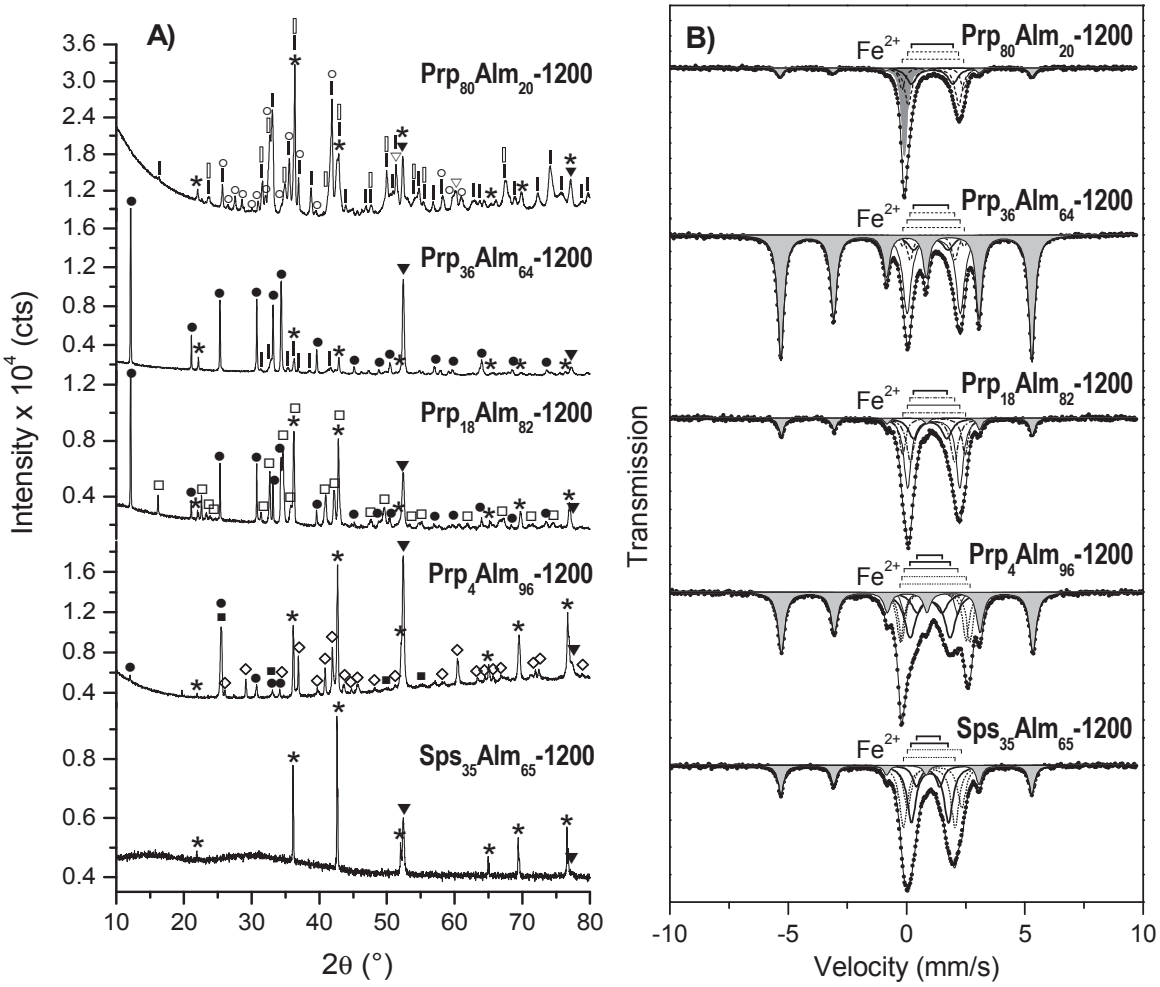

FIGURE 3. (A) XRD patterns showing the decomposition products of all the studied garnets after heating up to 1200 °C in reducing atmosphere. The symbols indicate the identified phases: Enstatite (|), clino-enstatite (▯), cordierite (●), hercynite-spinel (✱), alpha iron (▼), gamma iron (▽), anorthite (○), pigeonite (□), fayalite (◇), and cristobalite (■). (B) ^{57}Fe Mössbauer spectra of garnets heated up to 1200 °C. Shadowed sub-spectra correspond to α-Fe (light grey) and γ-Fe (dark grey). Doublets correspond to the other identified phases: Hercynite-spinel (thick solid line), Fe-enstatite (dashed line), cordierite (thin solid line), pigeonite (dash-dotted line), and olivine (dotted line).

Mechanism of Thermal Decomposition of Natural Fe-Bearing Garnets

XRD patterns of the samples after heating up to 1200 °C show different phase compositions (see Fig. 3a). Common phases present in all the samples include metallic iron and Fe-spinel ($(Fe,Mg)Al_2O_4$). The other identified

decomposition products are cristobalite (SiO_2), olivine (fayalite Fe_2SiO_4 or tephroite Mn_2SiO_4), Fe-cordierite ($(Fe,Mg)_2Al_4Si_5O_{18}$), pyroxene (enstatite $(Mg,Fe)SiO_3$ or pigeonite $((Mg,Fe^{2+},Ca)(Mg,Fe^{2+})Si_2O_6$), and anorthite ($CaAl_2Si_2O_8$) depending on the chemical composition of the starting garnet (all the phases are usually well crystallized). Anorthite and pigeonite were formed only if Ca was present in the dodecahedral site of the garnet structure. The Fe-bearing phases present in the samples of decomposed garnets were confirmed by ^{57}Fe Mössbauer spectroscopy (see Fig. 3b).

Sample with Composition Near to End-Member Pyrope (Prp)

The $Alm_{20}Prp_{80}$ sample, where Mg^{2+} cations predominantly occupy the dodecahedral sites and Fe^{2+} cations represent a minor contribution (X[Fe] = 0.465 apfu), was heated up to different temperatures (1100 °C, 1125 °C, and 1200 °C). At 1100 °C, the decomposition has already started, and the identified phases were zerovalent iron in two different crystallographic varieties, *i.e.*, bcc (α-Fe) and fcc (γ-Fe), the orthopyroxene enstatite ($(Mg,Fe)SiO_3$), and a predominant garnet (94.5%). At higher temperatures, 1125 °C and 1200 °C, besides iron and enstatite, we identified Fe-poor spinel ($(Mg,Fe^{2+})(Al,Cr,Fe^{3+})_2O_4$) and anorthite ($CaAl_2Si_2O_8$). In the XRD pattern of the sample heated up to 1125 °C, we also identified diffraction lines belonging to pyrope (48.1 wt%), indicating a slow decomposition of the garnet. The formation of anorthite was allowed due to the presence of Ca in the starting garnet. The pyroxene-enstatite, identified in the samples heated up to 1125 °C and 1200 °C is presented in two different polymorphs: orthoenstatite (*Pbca* space group) and clinoenstatite (*P*21/*c* space group) [27,28]. Because of the complexity and variety of the phase composition after decomposition, a XRD *in situ* measurement was carried out on the $Prp_{80}Alm_{20}$ sample under reducing atmosphere of forming gas between room temperature and 1200 °C.

Rietveld analysis was carried out on each diffractogram, recorded at elevated temperatures, in order to quantify the amount of each phase at the respective temperature. Quantitative results show that the decomposition process starts above 1000 °C, a result which agrees with the previous measurements (see above). The identified phases from *in situ* measurements are the same as those identified from the XRD patterns of the samples heated up to 1200 °C. Above 1000 °C, there is a progressive decrease of the weight percentage of the starting garnet at the expense of the decomposition products; indicating the slow rate of the reaction, where the decomposition process occurs in a wide temperature interval from 1080 to 1170 °C (ΔT = 90 °C) according to the DSC measurements. In the very beginning of thermal decomposition (1060 °C), the phases identified, besides garnet (98.3%), were: orthoenstatite and anorthite. On increasing the temperature from 1100 to 1200 °C, the decomposition products included anorthite, α-Fe, spinel, and enstatite. The identified enstatite was present in four polymorphs: orthoenstatite (*Pbca*), clinoenstatite low (*P*21/*c*), clinoenstatite high (*C*2/*c*), and protoenstatite (*P*21*cn*) [27,28].

From the ^{57}Fe Mössbauer spectra of the $Prp_{80}Alm_{20}$ sample, heated up to different temperatures (for details, see [19]), it was seen that before the decomposition onset (1087 °C), a slow reduction of Fe^{3+} in the octahedral sites occurs, which is a non-destructive process to the garnet structure that remains unaltered. In the ^{57}Fe Mössbauer spectra of the samples heated up to 1125 and 1200 °C (see Fig. 3b), two doublets (M1 and M2 octahedral sites) are assigned to enstatite. The Mössbauer parameters of enstatite for sites M1 (IS = 1.11–1.12 mm/s, QS = 2.59–2.60 mm/s) and M2 (IS = 1.14–1.17 mm/s, QS = 2.13 mm/s) reveals that enstatite is more likely to be orthorhombic and not monoclinic [29,30]; the sub-spectral M1/M2 area ratio varies with different temperatures indicating a variation in the site-occupancy of Fe^{2+} cations. One doublet (IS = 1.08–1.15 mm/s, QS = 1.70–1.75 mm/s) was assigned to Fe^{2+} in the tetrahedral sites of the hercynite-spinel.

As was seen from the ^{57}Fe Mössbauer spectra, the iron-bearing enstatite was only present in orthoenstatite; therefore, the identified clinoenstatite is iron-free. It is then possible to assume that a slow Fe^{2+} cation reduction in the octahedral sites of orthoenstite produce metallic iron, and against the "new" iron-free enstatite can recrystallize into clinoenstatite polymorph. This assumption is weakened by missing SiO_2 in the diffractograms. However, as we expect formation of just small amount of SiO_2, it can be hidden by the other crystalline phases or it can be amorphous. This hypothesis can be expressed by the equation given as

$$Mg_{1-x}Fe_xSiO_3 + xH_2 \rightarrow xFe + (1 - x)MgSiO_3 + xSiO_2 + xH_2O. \quad (1)$$

Summarizing all the aforementioned facts, the decomposition process of $Prp_{80}Alm_{20}$ sample between 1065 and 1200 °C can be expressed as:

$$Prp_{80}Alm_{20} + H_2 \rightarrow \text{Spinel} + (\alpha,\gamma)\text{-Iron} + (O, C)\text{-Enstatite} + \text{Anorthite} + H_2O.$$

Sample with Composition Near to End-Member Almandine (Alm)

The phase composition analysis shows the variety of the decomposition products of each garnet sample with different iron content in the dodecahedral sites. The sample with the major amount of iron cations in the dodecahedral sites (Prp_4Alm_{96}, X[Fe] = 2.845 apfu), when heated at higher temperatures than the decomposition temperature (1055 °C), *i.e.*, at 1070 and 1200 °C, shows a very similar phase composition, but with a different percentage contribution (see Fig. 4).The identified phases were: α-Fe, cristobalite (SiO_2), iron-end-member olivine (fayalite Fe_2SiO_4), and iron-rich cordierite ($(Fe,Mg)_2Al_4Si_5O_{18}$). The weight percentage variations in phase composition at different temperatures (see Fig. 4) indicate consecutive reactions of primary products of almandine decomposition as soon as they were formed: fayalite content increased (+ 13.1 wt%) at the expense of alpha iron (– 4.5 wt%) and cristobalite (– 11.5 wt%). Contents of hercynite and Fe-cordierite vary only slightly: hercynite content decreases and Fe-cordierite content increases.

Similar variation of phase percentages was found also in the ^{57}Fe Mössbauer spectra, where the sextet corresponding to α-Fe shows a decreased area when the sample was heated at 1200 °C (Fig. 3b) compared to temperature of 1070 °C (for detailed information, see [19,20]). Fayalite was fitted with two paramagnetic doublets (M1 and M2 octahedral sites), where the spectral ratio between the doublets, for both temperatures, was close to the unity. This result is close to the theoretical occupancy for iron in olivine structure [31]. The hyperfine parameters of two hercynite doublets (T1 and T2 tetrahedral sites) agree with those published for natural Fe-bearing spinel [32]. In the XRD patterns [20], a slight shift of hercynite diffractions of Prp_4Alm_{96} heated up to 1200 °C with respect to Prp_4Alm_{96} heated up to 1070 °C could be explained in terms of incorporation of extra iron into the hercynite or some grade of inversion of its structure, as the studied dependence of interplanar distance on iron content according to the Vegard's law in the hercynite-spinel series [33]. The most intense diffraction peak of Fe-cordierite (312) showed a shift towards larger *d*-values with increasing temperature of treatment. This variation in the cell parameters can be related to more iron atoms incorporated into the cordierite structure with increasing temperature [34].

The ilmenite inclusion in the Prp_4Alm_{96} sample decomposes into rutile and metallic iron at around 850 °C [20]. When the garnet decomposition occurs, there is a pronounced endothermic peak at 1055 °C and water vapor formation at 1075 °C. Then, the reaction of Prp_4Alm_{94} with hydrogen between 950 to 1200 °C can be described by the equation as

$$Fe_{2.85}Mg_{0.15}Al_2Si_3O_{12} + H_2 \rightarrow 0.90Fe_{1-x}Mg_xAl_2O_4 + Fe + 0.50Fe_2SiO_4 + 2.25SiO_2 + 0.05(Fe_{1-x}Mg_x)_2Al_4Si_5O_{18} + H_2;\ (0 \leq x \leq 1). \quad (2)$$

Considering $x = 0.15$, it is possible to calculate the theoretical mass loss from Eq. (2), which gives a value of – 3.21%. As explained in our previous work [20], fayalite and Fe-cordierite were formed by a secondary reaction between the primary products as the temperature increases (Eq. 3 and 4):

$$2\ Fe + SiO_2 + 2\ H_2O \rightarrow Fe_2SiO_4 + 2\ H_2, \quad (3)$$

$$2\ Fe_{1-x}Mg_xAl_2O_4 + 5\ SiO_2 \rightarrow (Fe_{1-x}Mg_x)_2Al_4Si_5O_{18}. \quad (4)$$

Based on the experimental data and previous equations, a general mechanism of reductive decomposition of almandine-close composition garnet can be expressed as

$$Fe_{3-x}Mg_xAl_2Si_3O_{12} + (2-b)H_2 \rightarrow (1-a)Fe_{1-x}Mg_xAl_2O_4 + (2-b)Fe + (b/2)Fe_2SiO_4 + (3-5a/2-b/2)SiO_2 + (a/2)(Fe_{1-x}Mg_x)_2Al_4Si_5O_{18} + (2-b)H_2O. \quad (5)$$

Fe-cordierite and fayalite are formed in amounts indicated as "*a*" and "*b*", respectively.

Samples with Intermediate Composition: Prp-Alm and Sps-Alm Solid Solutions

The sample with an intermediate composition, $Prp_{18}Alm_{82}$ (X[Fe] = 2.339 apfu), heated at high temperatures (1100 °C, 1115 °C, 1130 °C, and 1200 °C), show a similar phase composition for temperatures of 1130 and 1200 °C (see Fig. 4). At 1100 °C, the decomposition reaction is already initialized, and it was possible to identify α-Fe,

quartz (SiO_2), spinel-hercynite ($(Mg,Fe)Al_2O_4$), and a high percentage of garnet (87.8%). At 1115 °C, the phase composition is as follows: α-Fe, quartz-cristobalite (SiO_2), and spinel-hercynite, Fe-cordierite ($(Fe,Mg)_2Al_4Si_5O_{18}$), pigeonite ($(Mg,Fe,Ca)(Mg,Fe)Si_2O_6$), and garnet (64.7%).

At 1200 °C, all the garnet was completely decomposed, with decomposition products including α-Fe, spinel-hercynite, Fe-cordierite, and the Ca-poor pyroxene pigeonite. The slight percentage variation of spinel-hercynite, cristobalite, and Fe-cordierite, observed for the sample heated up to 1130 and 1200 °C (see Fig. 4), indicates that there is a secondary reaction taking place corresponding to the formation of Fe-cordierite. ^{57}Fe Mössbauer spectra (Fig. 3b) also confirm the presence of the bearing-iron phases: hercynite-spinel, iron, Fe-cordierite, and pigeonite.

For the above mentioned sample, the TG graph (not shown) has two distinct regions, *i.e.*, the first region when the sample is decomposed at 1109 °C, and the second region when a decreasing slope is observed suggesting the occurrence of a secondary reaction. Using the gathered data for this sample ($Prp_{18}Alm_{82}$) and including also the manganese cations in the decomposition model, it is possible to quantitative describe the reaction mechanism between 1024 and 1200 °C, *i.e.*,

$$Fe_{2.34}Mg_{0.5}Mn_{0.1}Ca_{0.06}Al_2Si_3O_{12} + 0.45H_2 \rightarrow 0.42Fe_{1-(x1+y1)}Mg_{x1}Mn_{y1}Al_2O_4 + 0.45Fe + 0.29(Fe_{1-(x1+y1)}Mg_{x1}Mn_{y1})_2Al_4Si_5O_{18} + 0.775Fe_{2-(x2+z1)}Mg_{x2}Ca_{z1}Si_2O_6 + 0.45H_2O. \quad (6)$$

In this specific case, $x1 = 0.3$, $x2 = 0.26$, $y1 = 0.1$, and $z1 = 0.08$. Using these values, the theoretical mass loss was calculated as – 1.51%. Until 1130 °C, SiO_2 was one of the decomposition products, and it reacted with spinel-hercynite to produce Fe-cordierite in a similar way as produced in Prp_4Alm_{96} sample, *i.e.*,

$$2Fe_{1-(x1+y1)}Mg_{x1}Mn_{y1}Al_2O_4 + 5SiO_2 \rightarrow (Fe_{1-(x1+y1)}Mg_{x2}Mn_{y1})_2Al_4Si_5O_{18}. \quad (7)$$

It is also possible to generalize the decomposition mechanism for $Prp_{18}Alm_{82}$, with "*d*" representing the formed amount of pigeonite, $x = x1 + dx2$, $y = y1$, and $z = dz1$, *i.e.*,

$$Fe_{3-(x+y+z)}Mg_xMn_yCa_zAl_2Si_3O_{12} + 2(1-d)H_2 \rightarrow ((4d-1)/5)Fe_{1-(x1+y1)}Mg_{x1}Mn_{y1}Al_2O_4 + 2(1-d)Fe + ((3-2d)/5)(Fe_{1-x1}Mg_{x1})_2Al_4Si_5O_{18} + dFe_{2-(x2+z1)}Mg_{x2}Ca_{z1}Si_2O_6 + 2(1-d)H_2O. \quad (8)$$

Another garnet with an intermediate composition, $Prp_{36}Alm_{64}$ (X[Fe] = 1.864 apfu), when heated above the decomposition temperature (1135 °C), has α-Fe, ortho-enstatite ($(Mg,Fe)SiO_3$), Fe-cordierite ($(Fe,Mg)_2Al_4Si_5O_{18}$), and hercynite-spinel ($(Mg,Fe)Al_2O_4$) as decomposition products. In this case, above the decomposition temperature, the garnet structure is completely destroyed and the endothermic reaction is of one-step character. However, careful observation of the percentage variation of phase composition at different temperatures (1150 °C, 1180 °C, and 1200 °C) suggest again consecutive reactions between the original decomposition products (see Fig. 4). There is a progressive rise, from 1150 °C to 1200 °C, in the weight percentage of Fe-cordierite (+ 27.8%) and α-Fe (+ 8.5%), and, at the same time, a decrease in the weight percentage of enstatite (– 24.4%) and hercynite-spinel (– 11.9%).

Together with the information on the phase composition, it was possible to suggest a relationship between the phases formed after $Prp_{36}Alm_{64}$ thermal decomposition between 942 °C and 1200 °C, *i.e.*,

$$Fe_{1.87}Mg_{1.13}Al_2Si_3O_{12} + 1.2H_2 \rightarrow 0.12Fe_{1-x2}Mg_{x2}Al_2O_4 + 1.2Fe + 0.80Fe_{1-x1}Mg_{x1}SiO_3 + 0.44Fe_{2-x3}Mg_{x3}Al_4Si_5O_{18} + 1.2H_2O. \quad (9)$$

If $x1 = 0.6$, $x2 = 0.8$, $x3 = 1.25$, the theoretical mass loss was calculated as – 4.13%. As it was mentioned above, cordierite and metallic iron weight percentages increase with the increasing temperature of heating, while enstatite and hercynite decrease. This suggests a consecutive reaction between the decomposition products, which can be expressed as

$$2Fe_{1-x2}Mg_{x2}Al_2O_4 + 5Fe_{1-x1}Mg_{x1}SiO_3 + 5H_2 \rightarrow 5Fe + Fe_{2-x3}Mg_{x3}Al_4Si_5O_{18} + 5H_2O. \quad (10)$$

If "*b*" representing the amount of formed enstatite is introduced, the mechanism of $Prp_{36}Alm_{64}$ decomposition can be generalized as

$$Fe_{3-x}Mg_xAl_2Si_3O_{12} + (2 - b)H_2 \rightarrow ((2b - 1)/5)Fe_{1-x2}Mg_{x2}Al_2O_4 + (2 - b)Fe + bFe_{1-x1}Mg_{x1}SiO_3 + ((3 - b)/5)Fe_{2-x3}Mg_{x3}Al_4Si_5O_{18} + (2 - b)H_2O \quad (11)$$

A garnet sample with an intermediate composition from the Alm-Sps series was also studied, *i.e.*, the $Sps_{35}Alm_{65}$ sample (X[Fe] = 1.946 apfu). It has a similar amount of Fe^{2+} cations as the $Prp_{36}Alm_{64}$ sample, but the decomposition process was quite different. From the XRD pattern of the sample heated up to 1120 °C, it is possible to see that decomposition has already started and the phases identified are: α-Fe, hercynite, tephroite ($(Mn,Fe)SiO_4$), quartz (SiO_2), and the original garnet (92.8%). However, when the sample is further heated up to 1140 and 1150 °C, the stronger diffraction lines belonging to hercynite (see Fig. 3a) appear, while the minor phases include garnet (only in the $Sps_{35}Alm_{65}$-1140 sample, 14.2%) and tephroite (in both samples); however, in the $2\theta = 20–35°$ region, there is a wide shoulder in the diffractogram that could be ascribed to an amorphous phase, most probably of silica (SiO_2) nature. In the sample heated up to 1200 °C, the only identified phases are α-Fe, hercynite, and amorphous component (see Fig. 3a).

In this particular case, because of the presence of amorphous phases in the XRD pattern, the quantitative analysis was complicated. Here, ^{57}Fe Mössbauer spectroscopy was a crucial tool to monitor the variation of phase composition with the temperature of heating and helped identify the amorphous component in $Sps_{35}Alm_{65}$-1200 sample. For the $Sps_{35}Alm_{65}$-1120 sample, the ^{57}Fe Mössbauer spectrum shows only a doublet corresponding to Fe^{2+} in an undecomposed garnet (91.7%), and a small sextet corresponding to α-Fe (8.3%). Almost identical ^{57}Fe Mössbauer spectra were obtained for samples heated up to 1140 °C, 1150 °C, and 1200 °C. Excluding the small Fe^{2+} doublet in garnet (with a spectral area of 2%) in the $Sps_{35}Alm_{65}$-1140 sample, all the spectra where fitted with one sextet for α-Fe, two doublets for Fe^{2+} in the octahedral sites of tephroite (M1 and M2) [35], and two doublets for Fe^{2+} in the tetrahedral sites of hercynite (T1 and T2) (Fig. 3b). From this, it is possible to identify that the amorphous phase in the XRD pattern of the $Sps_{35}Alm_{65}$-1200 sample was of melted tephroite origin, which is not a common case, as minerals typically melt congruently at high temperatures. Also from the ^{57}Fe Mössbauer spectra, it was noticed that the spectral areas of particular phases did not have a great variation between the samples heated at 1150 and 1200 °C, and it seems that there is not a subsequent secondary reaction occurring among the decomposition products.

It is worthwhile to mention that the TG curves show a gradual mass-loss starting from 970 °C, suggesting a gradual decomposition followed by melting of SiO_2 and tephroite. Taking into account these evidences, it is possible to quantitatively describe the decomposition mechanism as

$$Fe_{1.95}Mn_{1.05}Al_2Si_3O_{12} + 0.35H_2 \rightarrow FeAl_2O_4 + 0.35Fe + 0.825Mn_{2-x2}Fe_{x2}SiO_4 + 2.175SiO_2 + 0.35H_2O \quad (12)$$

where $x2 = 0.73$, and the calculated TG mass loss is – 1.13%.

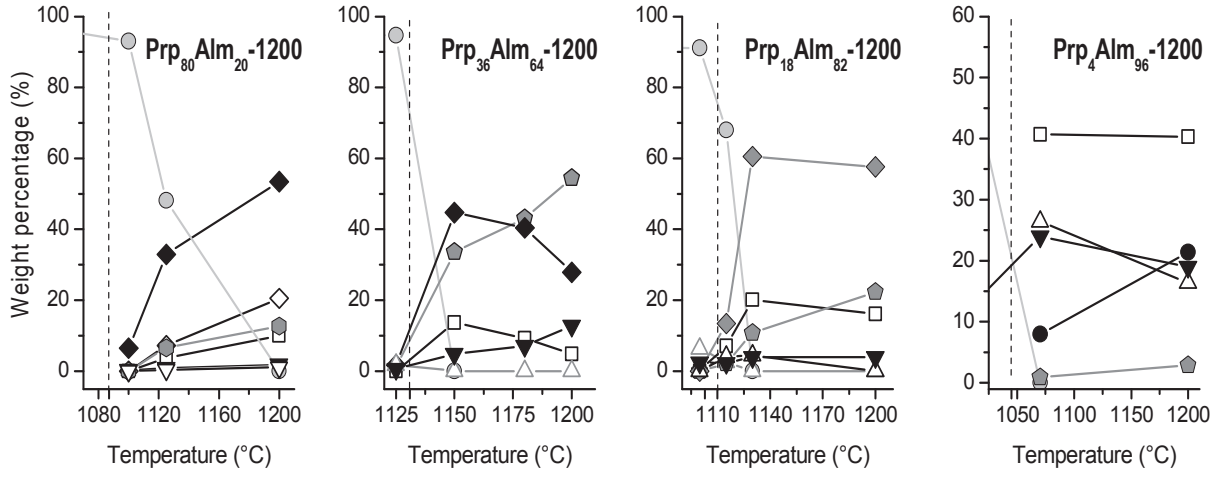

FIGURE 4. Graphs showing the relative weight fraction calculated by the Rietveld refinement for the samples heated up to 1200 °C. The symbols in the graphs represent the identified phases: Garnet (●), enstatite (◆), clinoenstatite (◇), hercynite-spinel (□), anorthite (⬢), alpha iron (▼), gamma iron (▽), cordierite (⬟), quartz (△), pigeonite (◆), cristobalite (△), and fayalite (●).

Table 2 summarizes the experimental and calculated values of TG mass loss after the thermal decomposition of garnets. The calculation took into account the mass losses from the beginning of decomposition, and the experimental value of water release before the decomposition was added. However, in the case of the $Prp_{80}Alm_{20}$ garnet, it was not possible to calculate the corresponding mass loss, because the decomposition mechanism could not be quantitatively described.

Morphology of Iron Particles Formed upon Decomposition of Garnets

The formation of metallic-iron particles was a common feature of the thermal decomposition of all the studied Fe-bearing garnets (see Fig. 5). The shape and size of these particles are variable, depending not only on the quantity of iron, but also on the whole set of phases formed during the garnet decomposition. The identification of the iron particles was possible by SEM in combination with energy-dispersive X-ray spectroscopy (EDS).

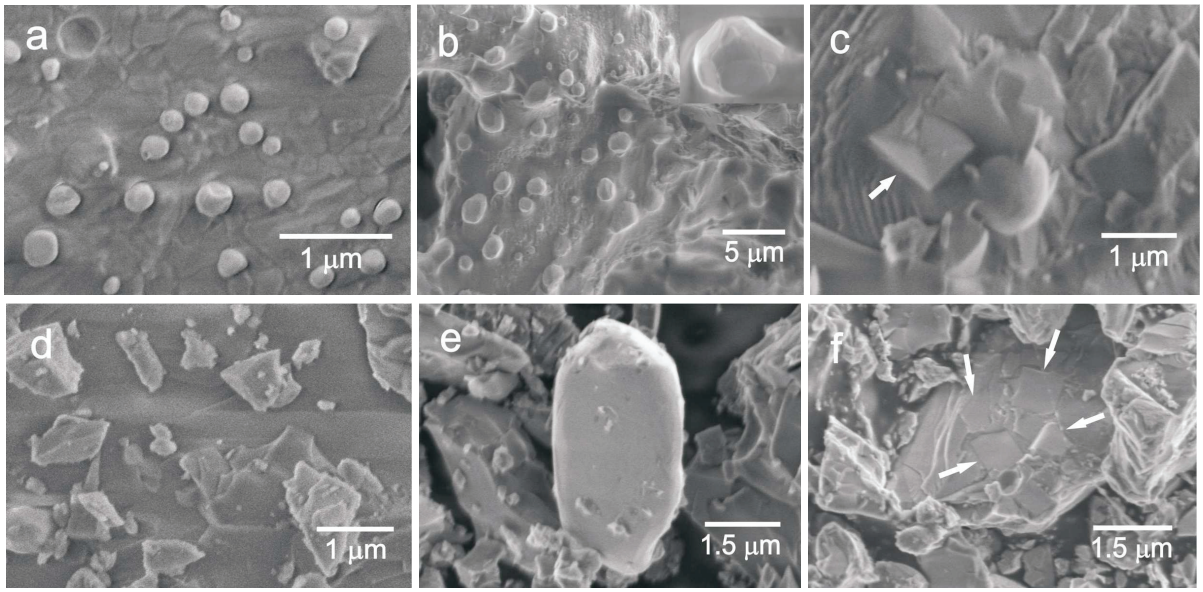

FIGURE 5. SEM photographs showing the morphology of iron particles formed upon garnet decomposition: (a) $Prp_{80}Alm_{20}$, (b) $Prp_{36}Alm_{64}$, (c) $Prp_{18}Alm_{82}$, (d) $Sps_{35}Alm_{65}$, (e) and (f) Prp_4Alm_{96}. The arrows point to the hercynite-spinel crystals.

In the $Prp_{80}Alm_{20}$-1200 sample, the small rounded iron particles have variable sizes (60–600 nm) and are spread almost uniformly over the mineral matrix, composed of spinel, anorthite, and enstatite. Note that the iron particles have a different crystallographic structure: bcc α-Fe and fcc γ-Fe. Based on the employed experimental approach, it is not possible to relate the size and morphology of the particles with the crystallographic structure of iron. Haneda *et al.* [36] suggest that fast cooling of ultrafine particles leads to retention of fcc lattice, while relatively large particles display a slow transformation into bcc lattice. However, De Caro *et al.* [37] proposed a critical size of 3 nm: below this threshold, the particles show a bcc structure, and above a fcc structure. Compared to our study, both authors used smaller particles for their studies and it is therefore not possible to relate their results with our observations.

Although the $Prp_{36}Alm_{64}$-1200 sample contains very well-defined micrometric iron particles (0.4–2 μm) similarly as in the $Prp_{80}Alm_{20}$-1200 sample, the iron particles have an irregular-polyhedral to almost rounded shape and are embedded in a mineral matrix of Fe-cordierite, Fe-enstatite, and hercynite-spinel nature.

In the $Prp_{18}Alm_{82}$ sample, the rounded iron particles (0.5–1 μm) appear along with the regular-octahedral crystals of hercynite with an edge of approximately 1 μm long. The formation of similar octahedral crystals of hercynite is known from high-temperature experiments under reducing atmosphere in the $FeO–Al_2O_3–SiO_2$ system [16].

Flat-elongated iron particles were found in the Prp_4Alm_{96}-1200 sample with variable lengths (3–5.5 μm) and width (2–2.5 μm). These particles are spread over the mixed-mineral matrix consisting of fayalite, cristobalite, and Fe-cordierite. Moreover, perfect cubic crystals of hercynite-spinel, which have an edge length of approximately 1 μm, were found embedded in this mineral matrix.

In contrast, it was not possible to identify any iron particles in the $Sps_{35}Alm_{65}$ sample, even when both XRD and ^{57}Fe Mössbauer spectroscopy confirmed their presence. The mineral matrix and the small objects on its surface have the same chemical composition according to EDS, and they were identified as hercynite, amorphous tephroite, and probably SiO_2. The iron particles are probably fully embedded in this mineral mixture.

CONCLUSIONS

All the studied garnets, when thermally treated under reduced conditions, have different onset temperature of decomposition, but always above 1000 °C. Although the garnets with different chemical composition have comparable crystal structure, the observed decomposition mechanism significantly differs. The main reason could be seen in the occupation of the dodecahedral sites with different cations, affecting the strength of inter-atomic bonds, and, consequently, the thermal stability of the structure. The formation of metallic iron upon reduction of ferric and ferrous cations under hydrogen atmosphere is confirmed to be a common feature of the garnet decomposition.

The common decomposition products observed for all the studied garnets include metallic iron (α-Fe, with particles size below 4 μm) and hercynite-spinel. Fe-cordierite is observed for garnets with iron occupancy in the dodecahedral sites between 1.864 and 2.845 atoms per formula unit (apfu). Other decomposition products are pyroxenes as enstatite and pigeonite for garnets with iron occupancy from 0.465 to 2.339 apfu, where pigeonite is formed only in presence of Ca cations. Olivines as fayalite and tephroite are formed only from $Alm_{96}Prp_4$ and $Alm_{65}Sps_{35}$ garnets. Cristobalite was only found after the Prp_4Alm_{96} decomposition; anorthite emerged after the decomposition of $Alm_{20}Prp_{80}$, where the Ca amount in the dodecahedral sites was significantly high.

The onset temperature of decomposition has a inverse linear dependence with the iron content in the dodecahedral sites of the garnet; the only exception is observed for pyrope, which has an onset temperature around 40 °C greater than for almandine, but it shows a slower decomposition rate than the other garnets. It could be driven by the presence of Ca in the dodecahedral sites; also Fe^{3+} and Cr in the octahedral sites could promote destabilization of the garnet structure.

The thermal stability of the garnets decreases with the increase of iron content, but when the iron content is very low, *i.e.*, for a garnet composition close to pyrope, the thermal stability decreases, but still it is greater than for almandine. Although this is contradictory to the linear tendency observed for the other garnets, it could probably be explained in terms of a local distortion induced by the presence of Ca in the *X*-sites.

In all the studied natural garnets, the molar fraction of the produced iron is the same as the molar fraction of hydrogen participating in the reaction. Therefore, it is possible to conclude that the amount of metallic iron formed upon thermal decomposition of Fe-bearing garnets does not depend on the initial iron occupancy in garnets, but depend on the efficient reaction with hydrogen.

ACKNOWLEDGMENTS

The authors gratefully acknowledge the support by the Operational Program Research and Development for Innovations – European Regional Development Fund (project CZ.1.05/2.1.00/03.0058), Operational Program Education for Competitiveness – European Social Fund (CZ.1.07/2.3.00/20.0017, CZ.1.07/2.3.00/20.0155, and CZ.1.07/2.3.00/20.0056) and Grant No. LH12079 of the Ministry of Education, Youth and Sports of the Czech Republic. The author also thanks to Zdeněk Marušák for TG/DSC measurements, Jiří Pechoušek for Mössbauer measurements, Klára Čépe for SEM images and EDS measurements, Radek Škoda for EMPA measurements, and Bohumil David for the high-temperature XRD.

REFERENCES

1. W. A. Deer, R.A. Howie, and J. Zussman, *Rock-Forming Minerals: Orthosilicates*, Second Geological Society, London, 1997, p. 932.
2. C. A. Geiger, "Spectroscopic Investigations Relating to the Structural, Crystal-Chemical and Lattice-Dynamic Properties of $(Fe^{2+},Mn^{2+},Mg,Ca)_3Al_2Si_3O_{12}$ Garnet: A Review and Analysis" in *EMU Notes Mineral. Vol. 6*, edited by A. Beran and E. Libowitzky, Eötvös University Press, Budapest, 2004, pp. 589–645.
3. R. R. Rapple, "Garnet" in *Ind. Miner. Rocks Commod. Mark. Uses*, edited by J. E. Kogel, N. C. Trivedi, J. M. Baker, and S. T. Krukowski, Society for Mining, Metallurgy and Exploration Inc., Littleton, CO, 2006, pp. 475–480.

4. K. K. Chatterjee, *Uses of Industrial Minerals, Rocks and Freshwater*, Nova Science Publisher Inc., New York, 2009, p. 584.
5. E. P. Meagher, *Am. Mineral.* **60**, 218 (1975).
6. G. A. Novak and G. V. Gibbs, *Am. Mineral.* **56**, 791 (1971).
7. C. Romano, B. T. Poe, N. Kreidie, and C. McCammon, *Am. Mineral.* **91**, 1371 (2006).
8. D. Zherebetskyy, S. Lebernegg, G. Amthauer, and M. Grodzicki, *Phys. Chem. Miner.* **39**, 351 (2012).
9. J. C. P. de Oliveira, M. I. da Costa Jr., W. H. Schreiner, and A. Vasquez, *J. Magn. Magn. Mater.* **79**, 1 (1989).
10. C. A. Geiger, *Mineral. Petrol.* **66**, 271 (1999).
11. L. M. Anovitz, E. J. Essene, G. W. Metz, S. R. Bohlen, E. F. Westrum Jr., and B. S. Hemingway, *Geochim. Cosmochim. Acta* **57**, 4191 (1993).
12. Q. Zang, M. Enami, and K. Suwa, *Eur. J. Mineral.* **5**, 153 (1993).
13. L. Thiéblot, J. Roux, and P. Richet, *Eur. J. Mineral.* **10**, 7 (1998).
14. K. Barcova, M. Mashlan, R. Zboril, P. Martinec, and P. Kula, *Czechoslov. J. Phys.* **51**, 749 (2001).
15. R. Zboril, M. Mashlan, K. Barcova, and M. Vujtek, *Hyperfine Interact.* **139/140**, 597 (2002).
16. J. F. Schairer and K. Yagi, *Am. J. Sci.* **250-A**, 471 (1952).
17. R. Zboril, M. Mashlan, L. Machala, J. Walla, K. Barcova, and P. Martinec, *Hyperfine Interact.* **156/157**, 403 (2004).
18. R. Zboril, M. Mashlan, K. Barcova, J. Walla, E. Ferrow, and P. Martinec, *Phys. Chem. Miner.* **30**, 620 (2003).
19. C. Aparicio, J. Filip, and M. Mashlan, "High Temperature Decomposition of Almandine and Pyrope in Reducing Atmosphere" in *Mössbauer Spectroscopy in Materials Science - 2010*, edited by J. Tucek and M. Miglierini, AIP Conference Proceedings Vol. 1258, American Institute of Physics, Melville, NY, 2010, pp. 47–54.
20. C. Aparicio, J. Filip, H. Skogby, Z. Marusak, M. Mashlan, and R. Zboril, *Phys. Chem. Miner.* **39**, 311 (2012).
21. J. L. Pouchou and F. Pichoir, *Microbeam Anal.* **20**, 104 (1985).
22. G. Amthauer, H. Annersten, and S. S. Hafner, *Zeitschrift für Krist.* **143**, 14 (1976).
23. C. A. Geiger, M. Grodzicki, and G. Amthauer, *Phys. Chem. Miner.* **30**, 280 (2003).
24. A. Bosenick, M. T. Dove, and C. A. Geiger, *Phys. Chem. Miner.* **27**, 398 (2000).
25. C. A. Geiger, *Am. Mineral.* **93**, 360 (2008).
26. M. Merli, A. Callegari, E. Cannillo, F. Caucia, M. Leona, R. Oberti, and L. Ungaretti, *Eur. J. Mineral.* **7**, 1239 (1995).
27. N. Choudhury and S. L. Chaplot, *Solid State Commun.* **114**, 127 (2000).
28. J. R. Smyth, *Am. Mineral.* **59**, 345 (1974).
29. M. D. Dyar, R. L. Klima, D. Lindsley, and C. M. Pieters, *Am. Mineral.* **92**, 424 (2007).
30. S. G. Eeckhout, E. De Grave, C. A. McCammon, and R. Vochten, *Am. Mineral.* **85**, 943 (2000).
31. M. D. Dyar, E. C. Sklute, O. N. Menzies, P. A. Bland, D. Lindsley, T. Glotch, M. D. Lane, M. W. Schaefer, B. Wopenka, R. Klima, J. L. Bishop, T. Hiroi, C. Pieters, and J. Sunshine, *Am. Mineral.* **94**, 883 (2009).
32. S. Carbonin, U. Russo, and A. Della Giusta, *Mineral. Mag.* **60**, 355 (1996).
33. G. B. Andreozzi and S. Lucchesi, *Am. Mineral.* **87**, 1113 (2002).
34. T. Malcherek, M. C. Domeneghetti, V. Tazzoli, L. Ottonoli, C. McCammon, and M. A. Carpenter, *Am. Mineral.* **86**, 66 (2001).
35. H. Annersten, J. Adetunji, and A. Fillippidis, *Am. Mineral.* **69**, 1110 (1984).
36. K. Haneda, Z. X. Zhou, A. H. Morrish, T. Majima, and T. Miyahara, *Phys. Rev. B* **46**, 13832 (1992).
37. D. de Caro, T. O. Ely, A. Mari, B. Chaudret, E. Snoeck, M. Respaud, J.-M. Broto, and A. Fert, *Chem. Mater.* **8**, 1987 (1996).